Automatic Correction of Nonanechoic Antenna Measurements Using Complex Morlet Wavelets

Adrian Bekasiewicz, *Senior Member, IEEE*, and Vorya Waladi

***Abstract*—Real-world performance of antennas is normally tested in anechoic chambers (ACs). Alternatively, experimental validation can be performed in nonanechoic environments and refined in the course of postprocessing. Unfortunately, the existing methods are difficult to setup and prone to failure. In this letter, a wavelet-based framework for correction of nonanechoic antenna measurements has been proposed. The method involves automatic centering and adjusting of the wavelet w.r.t. a fraction of the signal that corresponds to line-of-sight transmission within the system under test. The performance of the method has been verified using two compact antennas and a total of 15 experiments. Benchmarks against the state-of-the-art approaches have also been performed.**

***Index Terms*—Anechoic chamber, measurements, compact antennas, nonanechoic tests, radiation pattern, wavelets.**

I. Introduction

MEASUREMENT of real-world performance is an inherent step of antenna development. Far-field characteristics are normally extracted from S_{21} transmission between the antenna under test (AUT) and the reference antenna (RA) in strictly controlled propagation conditions that ensure high quality of the results. In practice, the tests are often conducted in anechoic chambers (ACs) or compact range sites [1], [2]. Although professional antenna laboratories are capable of ensuring certification-grade measurement results, they are prohibitively expensive. Consequently, their construction/use for applications, such as training or low budget research might be unjustified. For the mentioned scenarios, the main goal is to ensure that the experimental data resemble simulations [3], [4], [5], [6], [7], [8].

The measurement cost can be substantially reduced by neglecting the use of specialized facilities in favor of installing the test equipment in the nonanechoic (NA) sites, e.g., offices, hallways, or courtyards [9], [10], [11], [12], [13]. Unfortunately, multipath interferences and a random noise from the external sources of electromagnetic (EM) radiation make the responses obtained in such conditions useless for drawing conclusions on the antenna far-field performance [9]. The problem can be addressed through appropriate postprocessing. Suitable techniques are based on, e.g., one-shot multifrequency measurements, or test site characterization [10], [11], [16], [21]. The first class comprises time-domain methods, where the fraction of the RA-AUT signal that corresponds to the line-of-sight (LoS) transmission is extracted from noisy responses [12], [13]. Postprocessing can also be performed using the spectral approaches [22], [23]. Unfortunately, the performance of considered methods is subject to setup of multiple parameters (derived as a result of manual or semimanual tuning) [14], [15], [16]. The second class of methods involves extraction of the test site propagation conditions based on a series of experiments performed in the predetermined locations of the RA-AUT system, and/or through filtration of the environmental noise [10], [11], [13]. However, the need for multiple measurements makes these techniques difficult to setup [10]. Moreover, their performance might be affected by temporal dynamics of the environment [11]. The mentioned difficulties limit usefulness of the existing methods for day-to-day antenna measurements.

In this letter, a wavelet-based framework for correction of NA antenna measurements has been proposed. The method combines anglewise extraction of the LoS delay profile from the RA-AUT system with automatic tuning of the Morlet wavelets around the relevant part of the transmission. Apart from the use of wavelets, the contributions of the work include: analysis of time-domain RA-AUT signals in the form of power responses, automatic extraction of LoS profiles, and their use for optimization of wavelet functions. Performance of the presented method has been demonstrated using two geometrically small antennas. Benchmark results indicate that the approach offers up to almost 9 dB better correction performance when compared against the existing techniques.

II. Methodology

A. Problem Formulation

Let $\boldsymbol{R}_u(\boldsymbol{\omega}, \boldsymbol{\theta})$ be the matrix of uncorrected, complex S_{21} responses measured in the NA test site, where $\boldsymbol{\omega} = [\omega_1 \ \ldots \ \omega_k]^T$, $k = 1, \ldots, K$, represents the sweep around the frequency of interest $f_0 = (\omega_K - \omega_1)/2$; $\boldsymbol{\theta} = [\theta_1 \ \ldots \ \theta_a]^T$, $a = 1, ..., A$, is the angular position of AUT w.r.t. RA, and $B = \omega_K - \omega_1$ is the bandwidth around f_0. The vector $\boldsymbol{R}_c(f_0, \boldsymbol{\theta})$ denotes the refined radiation pattern. The goal of correction is to transform the noisy data $\boldsymbol{R}_u(\boldsymbol{\omega}, \boldsymbol{\theta})$ using complex Morlet wavelets so as to extract $\boldsymbol{R}_c(f_0, \boldsymbol{\theta})$ that approximates the AC measurements.

B. Automatic Extraction of LoS Delay Profile

Let $\boldsymbol{T}_u = \boldsymbol{T}_u(\boldsymbol{t}, \theta_a) = \mathscr{F}^{-1}(\boldsymbol{R}_u, N)$ be the complex time-domain response at θ_a angle obtained from $\boldsymbol{R}_u = \boldsymbol{R}_u(\boldsymbol{\omega}, \theta_a)$ using inverse Fourier transform [denoted as $\mathscr{F}^{-1}(\cdot)$], where $\boldsymbol{t} = [t_1, \ldots, t_N]^T = \partial t \cdot \boldsymbol{M}$ with $\partial t = B^{-1}$, $\boldsymbol{M} = [-N/2, \ldots, N/2-2, N/2-1]^T$, and $N = 2^{\lceil \log 2(K) \rceil + 3}$, respectively [13], [17]. Then, let $\boldsymbol{P} = \boldsymbol{P}(\boldsymbol{t}, \theta_a) = \boldsymbol{T}_u \circ \boldsymbol{T}_u^*$ be the power response in

Manuscript received 15 March 2024; accepted 7 May 2024. Date of publication 9 May 2024; date of current version 6 August 2024. This work was supported in part by the National Science Centre of Poland under Grant 2021/43/B/ST7/01856 and in part by the Gdansk University of Technology (Excellence Initiative—Research University) under Grant 16/2023/IDUB/IV.2/EUROPIUM. *(Corresponding author: Adrian Bekasiewicz.)*

The authors are with the Faculty of Electronics, Telecommunications and Informatics, Gdansk University of Technology, 80-233 Gdansk, Poland (e-mail: adrian.bekasiewicz@pg.edu.pl).

Digital Object Identifier 10.1109/LAWP.2024.3398656

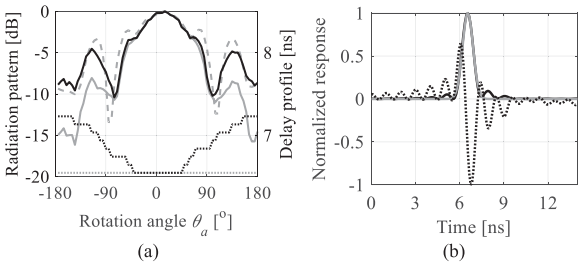

Fig. 1. NA measurements: (a) AC-based (– –) versus corrected responses with variable (black) and constant (gray) LoS-profiles (···), as well as (b) normalized (optimized) Gaussian pulse (gray), power (–), and amplitude responses (···). Note that the former two are virtually the same for the LoS peak.

time domain (note that "$\circ$" and "*" are the componentwise multiplication and conjugate transpose) [18]. Normally, the time-domain responses are in the form of $\boldsymbol{T}_u$ or $|\boldsymbol{T}_u|$, which—due to ambiguity of signal changes—make them more challenging to analyze compared with $\boldsymbol{P}$ [12], [13], [14], [15]. Here, $\boldsymbol{P}$ is used to identify the RA-AUT maxima pertinent to the LoS delay. Note that—for, e.g., end-fire antennas—the RA-AUT distance is subject to change as a function of θ_a. As shown in Fig. 1(a), despite being subtle (time-wise), the mentioned variations affect the correction performance. Therefore, fidelity of the refined NA responses can be further improved by incorporating LoS versus $\boldsymbol{\theta}$ to the postprocessing. The delay profile aids selection of tight time-domain intervals.

The profile is extracted as follows. First, a vector of delays $\boldsymbol{d}_r{}^{(j)} = [d_{r.1}{}^{(j)} \ldots d_{r.a}{}^{(j)}]^T (j = 1)$ is defined, where

$$d_{r.a}^{(j)} = \underset{d_{r.a} \in \boldsymbol{t}: d_l \le d_{r.a} \le d_h}{\arg\max} \left(\boldsymbol{P}\left(\boldsymbol{t}, \theta_a\right)\right). \tag{1}$$

Here, $d_l = 0$ and $d_h = \partial t \cdot (N/2–1)$. Due to challenging propagation conditions in rudimentary NA sites, $\boldsymbol{d}_r{}^{(1)}$ might not represent the LoS delay with sufficient precision. This is because—for certain antennas and/or environments—the amplitude of reflected, non-LoS responses might be higher than for LoS. As an example, consider a directional radiator for which LoS part of signal at θ_a is at the radiation null, whereas its non-LoS component (associated with the main lobe) is reflected from a metallic surface [13]. Here, the problem of incorrect LoS estimation is mitigated through re-set ($j = 2$) of the profile $\boldsymbol{d}_r{}^{(2)}$ using (1) with bounds confined around $d_0 = \min(\boldsymbol{d}_r{}^{(1)})$ such that $d_l = d_0 - \alpha \cdot w_0$ and $d_h = d_0 + \alpha \cdot w_0$; w_0 denotes half-prominence (i.e., width at half of the height) of the power pulse $\boldsymbol{P}(t, \theta_0)$ [18], where θ_0 is the angular location of AUT that corresponds to d_0. Here, the scaling factor is set to $\alpha = 3$.

The rationale behind restricting the LoS search around d_0 is that the expected change of the RA-AUT distance (and hence delay) due to the AUT rotation is small [11], [13]. At the same time, w_0 is a function of the AUT at hand, as well as the selected B, and it is short enough to mitigate the risk that $\boldsymbol{d}_r{}^{(2)}$ will include incorrectly identified interferences as the LoS signal. Note that $\boldsymbol{d}_r{}^{(2)}$ only approximates the true delay due to distortions resulting from random external EM noise, as well as numerical errors [15]. The latter result not only from aliasing, but also zero-padding with $N > K$ (cf., Section II-A) [13], [15].

Distortions are reduced by modification of the LoS-profile using a median filter with smoothing function. First, the elements of the $\boldsymbol{d}_r{}^{(3)}$ vector ($j = 3$) are obtained as

$$d_{r.a}^{(3)} = \begin{cases} 1/2 \left(d_{r.a-1}^{(2)} + d_{r.a+1}^{(2)} \right), & \text{if } d_{r.a}^{(2)} \le M\left(\boldsymbol{d}_r^{(2)}\right) - 2\sigma\left(\boldsymbol{d}_r^{(2)}\right) \\ 1/2 \left(d_{r.a-1}^{(2)} + d_{r.a+1}^{(2)} \right), & \text{if } d_{r.a}^{(2)} \ge M\left(\boldsymbol{d}_r^{(2)}\right) + 2\sigma\left(\boldsymbol{d}_r^{(2)}\right) \\ d_{r.a}^{(2)}, & \text{otherwise} \end{cases} \tag{2}$$

where $M(\cdot)$ and $\sigma(\cdot)$ represent the median and standard deviation operations, respectively. The role of (2) is to alter the extracted LoS-profile at the θ_a angles for which the delay exceeds two standard deviations w.r.t. the median of the $\boldsymbol{d}_r{}^{(2)}$ vector.

The final profile, i.e., $\boldsymbol{d}_r{}^* = \boldsymbol{d}_r{}^{(4)} (j = 4)$ is constructed form convex combinations of the median-filtered elements

$$d_{r.a}^{(j)} = \frac{1}{2p+1} \sum_{i=a-p}^{a+p} d_{r.i}^{(j-1)} \tag{3}$$

where p represents a range of points around $d_{r.a}{}^{(j-1)}$ (here, $p = 2$ is set to balance "smoothness" and "dynamics" of profile changes with θ_a). Assuming availability of the $\boldsymbol{R}_u(\boldsymbol{\omega}, \boldsymbol{\theta})$ obtained for f_0, K, B, and N, the discussed algorithm is follows:

1) set $j = 1$ and extract $\boldsymbol{d}_r{}^{(j)}$ from $\boldsymbol{P}(\boldsymbol{t}, \theta_a)$ vectors using (1) with $d_l = 0$, and $d_h = \partial t \cdot (N/2–1)$;
2) find d_0, w_0, and θ_0, set $d_l = d_0 - \alpha \cdot w_0$, $d_h = d_0 + \alpha \cdot w_0$, and $j = j + 1$, and re-set $\boldsymbol{d}_r{}^{(j)}$ from $\boldsymbol{P}(\boldsymbol{t}, \theta_a)$, using (1);
3) set $j = j + 1$ and obtain $\boldsymbol{d}_r{}^{(j)}$ through application of median filter (2) to components from $\boldsymbol{d}_r{}^{(j-1)}$;
4) set $j = j + 1$ and obtain $\boldsymbol{d}_r{}^* = \boldsymbol{d}_r{}^{(j)}$ through alteration of elements from $\boldsymbol{d}_r{}^{(j-1)}$ using (3); END.

The automatic LoS-profile extraction enables accurate correction of measurements in NA regime using Morlet wavelets.

C. Response Correction Using Complex Morlet Wavelets

The motivation behind application of complex wavelets to postprocessing is shown in Fig. 1(b), which compares the time-domain amplitude and power responses extracted from the example RA-AUT measurement against a Gaussian function (all normalized). Note that the latter highly resembles the LoS part of the power pulse. The plots show that the analysis of $\boldsymbol{P}(\boldsymbol{t}, \theta_a)$ is suitable for identification of the interval pertinent to LoS transmission, which might be difficult when only $\boldsymbol{T}_u(\boldsymbol{t}, \theta_a)$ is available. Moreover, application of the complex wavelets to the complex time-domain signal maximizes the amount of data that can be extracted form one-shot measurement [18].

The wavelet kernel is composed of the complex exponential function and the Gaussian curve. It takes the following form:

$$\boldsymbol{T}_w\left(\boldsymbol{t}, \theta_a\right) = \exp\left(2\left(j\boldsymbol{Q} - \left(\boldsymbol{Q}\, w_w^{-1}\right)^2\right)\right) \tag{4}$$

where w_w is the number of cycles (that affects the wavelet width) and $\boldsymbol{Q} = \pi f_0 \left(\boldsymbol{t} - d_{r.a}^*\right)$. It should be noted that—as can be implied from (1)—variability of the $\boldsymbol{T}_w = \boldsymbol{T}_w(\boldsymbol{t}, \theta_a)$ kernel with θ_a is implicit as the change of AUT angular position affects the time-delay $d_{r.a}{}^*$ pertinent to direct transmission (cf., Section II-B). In other words, the ath element of $\boldsymbol{d}_r{}^*$ vector can be used to center the wavelet around the fraction of the impulse response $\boldsymbol{T}_u(\boldsymbol{t}, \theta_a)$ that corresponds to the LoS delay extracted from $\boldsymbol{P}(\boldsymbol{t}, \theta_a)$.

Appropriate width of the wavelet (from the standpoint of capturing the relevant part of the $\boldsymbol{T}_u$ response) is determined by solving the following curve-fitting problem:

$$w_w^* = \arg\min\left(U\left(w_w, f_0, \theta_0\right)\right) \tag{5}$$

where U is a scalar, least-square objective function of the form

$$U\left(w_w, f_0, \theta_0\right) = \sum\left(\boldsymbol{P}_\varepsilon\left(\boldsymbol{t}, \theta_0\right) - \boldsymbol{G}\left(w_w, \boldsymbol{t}, \theta_0, f_0\right)\right)^2 \tag{6}$$

$$\boldsymbol{G}\left(w_w, \boldsymbol{t}, \theta_0, f_0\right) = \exp\left(-2\left(\left(\pi f_0\left(\boldsymbol{t} - d_0\right)\right) w_w^{-1}\right)^2\right). \tag{7}$$

Here, $\boldsymbol{P}_\varepsilon = \boldsymbol{P}/\max(\boldsymbol{P})$ is a normalized power response. Note that d_0 in (7) is implicitly related to θ_0, which has been extracted during LoS-profile identification (see Section II-B). The goal of (5) is to find $w_w{}^*$ that minimizes the discrepancy between the Gaussian pulse and the fraction of the power response $\boldsymbol{P}(\boldsymbol{t}, \theta_0)$ that corresponds to the LoS signal. The obtained value is then used to setup the wavelet kernel (4). Note that the cost of (5) is negligible as it is executed only at θ_0. The reason for single-angle tuning is that, contrary to LoS-profile, the width of $\boldsymbol{P}$ does not vary much with θ_a. Hence, adjustment of (4) using $w_w{}^*$ ensures tight confinement of the RA-AUT response (LoS part of the signal) while mitigating the challenges related to limited-reliability of curve-fitting at θ_a angles with low signal-to-noise ratios (e.g., the end-fire AUT positioned backwards w.r.t. RA).

Next, the kernel (4), adjusted according to the $\boldsymbol{P}(\boldsymbol{t}, \theta_a)$, is used to find the frequency response $\boldsymbol{R}_c(\boldsymbol{\Omega}, \theta_a) = \mathscr{F}(\boldsymbol{T}_u(\boldsymbol{t}, \theta_a) \circ \boldsymbol{T}_w(\boldsymbol{t}, \theta_a), N)$ using a Fourier transform [here, $\mathscr{F}(\cdot)$], where $\boldsymbol{\Omega} = \partial\omega \cdot \boldsymbol{M} - B + f_0$, and $\partial\omega = (t_N - t_1)^{-1}$, respectively. The final, corrected NA transmission within the RA-AUT system at the frequency of interest $f_0 \in \boldsymbol{\Omega}$ (note that $\boldsymbol{\omega} \in \boldsymbol{\Omega}$) and angle θ_a is of the form of $R_c(f_0, \theta_a)$. In order to extract, $\boldsymbol{R}_c(f_0, \boldsymbol{\theta})$ the above-outlined procedure is executed at all θ_a angles.

D. Algorithm Summary

The presented wavelet-based framework for correction of NA measurements can be summarized as follows.

1) Set f_0, K, B, and N, and obtain $\boldsymbol{R}_u(\boldsymbol{\omega}, \boldsymbol{\theta})$ data.
2) Extract $\boldsymbol{d}_r{}^*$, d_0, and θ_0 using the algorithm of Section II-C.
3) Define (4) based on $w_w{}^*$ optimized using (5); set $a = 1$.
4) Determine $\boldsymbol{R}_c(\boldsymbol{\Omega}, \theta_a)$ and extract ath element $R_c(f_0, \theta_a)$ of $\boldsymbol{R}_c(f_0, \boldsymbol{\theta})$ vector.
5) If $a = A$, END; otherwise, set $a = a + 1$ and go to Step 4.

The vector $\boldsymbol{R}_c(f_0, \boldsymbol{\theta})$ is the corrected radiation pattern of the AUT. It is worth noting that the final postprocessing steps involve normalization of $\boldsymbol{R}_c$ followed by its conversion to decibels. It should be reiterated that the presented correction approach is based on a series of A one-shot measurements. Furthermore, tuning of the wavelet kernels does not require engineering insight. Consequently, the proposed framework provides a substantial improvement (setup-wise) compared with the state-of-the-art correction methods [12], [13], [14], [15].

III. Correction Results and Benchmark

The presented postprocessing framework has been demonstrated using an antipodal Vivaldi antenna and a spline-based monopole [13], [19]. The reference responses for both structures have been obtained in the AC. The NA RA-AUT data have been acquired in a 5.5 m × 4.5 m × 3.1 m test site of Fig. 2(a). The room is not dedicated to far-field experiments. Note that the Vivaldi structure is also used as the RA. The angular resolution of the measurements is set to 5° and the number of frequency points around f_0 is $K = 201$.

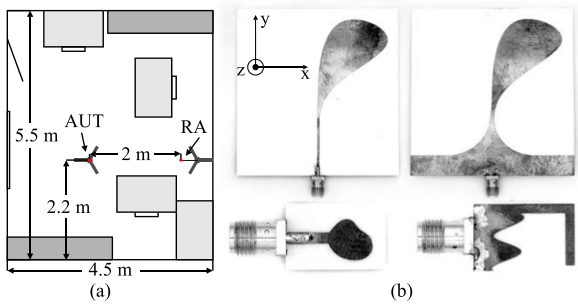

Fig. 2. Benchmark. (a) Schematic view of the NA test size with highlight on short/tall furniture (light/dark gray), and rotary towers with antenna mounts (red dots), as well as (b) photographs of the Vivaldi structure (top) and spline-based monopole (bottom) used for experiments (not in-scale).

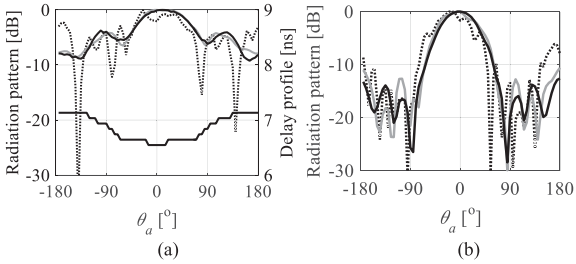

Fig. 3. Vivaldi antenna—AC-based patterns (gray) and the NA responses before (···), and after (–) correction at: (a) 4 GHz (with highlight on LoS delay profile—black) and (b) 8 GHz frequencies.

TABLE I
Vivaldi: Far-Field Correction Performance

f_0 [GHz]	3	4	5	6	7	8	9	10	11
$e_R(\boldsymbol{R}(f_0,\boldsymbol{\theta}))$ [dB]	−12.9	−15.2	−10.9	−12.2	−16.1	−17.5	−17.1	−16.5	−15.1
$e_R(\boldsymbol{R}_c(f_0,\boldsymbol{\theta}))$ [dB]	−23.6	−28.8	−21.9	−19.3	−24.8	−25.1	−24.3	−22.1	−22.3
$\Delta^{\#}$ [dB]	10.7	13.6	11.0	7.1	8.7	7.6	7.2	5.6	7.2

$^{\#}$ $\Delta = \left|e_R(\boldsymbol{R}_c(f_0,\boldsymbol{\theta})) - e_R(\boldsymbol{R}(f_0,\boldsymbol{\theta}))\right|$

A. Case Study I: Antipodal Vivaldi Antenna

The first case study involves measurements (in yz-plane) of the Vivaldi antenna, as shown in Fig. 2(b) [13]. The tests have been performed at $f_0 \in \{3, 4, 5, 6, 7, 8, 9, 10, 11\}$ GHz with rule-of-thumb-based bandwidth $B = 1$ GHz [13], [14]. Note that the correction is executed separately at each frequency.

After data acquisition, the LoS delay has been obtained using the heuristic of Section II-B. The example profiles extracted at 5 and 4 GHz are shown in Figs. 1(a) and 3(a), respectively. It should be emphasized that variations of the delay in $\boldsymbol{d}_r{}^*$—pertinent to the LoS transmission—are due to the antenna being attached perpendicular to the axis of rotation. Consequently, the RA-AUT distance fluctuate by around 0.2 m (i.e., from 1.96 m at 0° to 2.17 m at 180°) with θ_a angle. Next, the wavelet kernel is tuned using (5). Upon the optimization, the function (4) is centered (individually w.r.t. each θ_a angle) according to the extracted $\boldsymbol{d}_r{}^*$ vector. Finally, the $\boldsymbol{T}_w(\boldsymbol{t}, \theta_a)$ kernels are convolved with the original frequency responses and the refined radiation patterns $\boldsymbol{R}_c(f_0, \theta)$ are obtained as explained in Section II-C.

The antenna performance before and after correction—expressed in terms of the decibel-based root-mean-square error e_R calculated w.r.t. the AC data [15]—is summarized in Table I, whereas the radiation patterns at the selected frequencies are

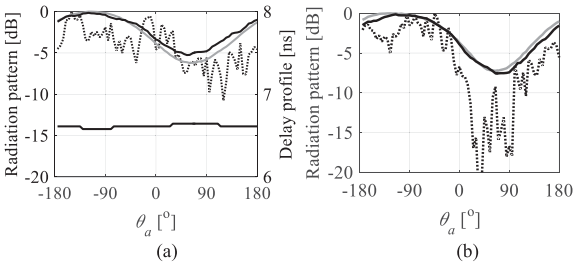

Fig. 4. Spline monopole—AC-based patterns (gray) and the NA responses before (···), and after (–) correction at: (a) 5 GHz (with highlight on LoS delay profile—black) and (b) 7 GHz frequencies.

TABLE II
MONOPOLE: FAR-FIELD CORRECTION RESULTS

f_0 [GHz]	4	5	6	7	8	9
$e_R(\boldsymbol{R}(f_0,\boldsymbol{\theta}))$ [dB]	–8.8	–14.1	–9.9	–12.8	–14.2	–10.7
$e_R(\boldsymbol{R}_c(f_0,\boldsymbol{\theta}))$ [dB]	–25.8	–26.2	–21.8	–28.1	–22.7	–20.5
Δ [dB]	–17	–12.1	–11.9	–15.3	–8.5	–9.8

shown in Fig. 3. The results indicate that the average improvement of the NA responses due to the proposed scheme amounts to 8.7 dB, i.e., from the average e_R of –14.8 dB to –23.6 dB, respectively. Note that the refinement quality can also be expressed in terms of, e.g., equivalent error signal [24].

B. Case Study II—Spline-Based Monopole

Consider a spline-based monopole of Fig. 2(c) [13]. The structure far-field performance has been characterized (in yz-plane; cf., Fig. 2) at $f_0 \in \{4, 5, 6, 7, 8, 9\}$ GHz with rule-of-thumb $B = 3$ GHz [13], [14]. The example LoS-profile for the antenna [cf., Fig. 4(a)] is much less nonlinear compared with the Vivaldi because the radiator is mounted at its axis of rotation.

The antenna correction results are summarized in Table II, whereas a comparison of the selected patterns before and after the refinement w.r.t. ac characteristics is shown in Fig. 4. The quality of the corrected responses at the considered test frequencies is high. Overall, the average e_R improved by a total of 12.4 dB, i.e., from –12.4 dB to –24.2 dB, respectively.

C. Discussion and Comparisons

The proposed framework has been compared against the time-gating and matrix-pencil (MP) methods. The intervals for the former are selected based on the following: (i) manual measurements of LoS and non-LoS distances (rectangular window [17]; obtained non-LoS distance: 4.1 m—delay: 13.7 ns) [14]; (ii) visual inspection of the impulse response (Hann window [17]; estimated non-LoS delay: 12 and 10 ns for Vivaldi and monopole, respectively) [15]; (iii) identification of the interval based on analysis of the time-domain signal at a selected θ_a angle (composite window function) [11]; (iv) for the MP method, the pencil parameter and the number of exponentials are set to 0.5 K and 3, respectively [14], [22].

Coefficients f_0, K, and B for all of the methods are the same as in Sections III-A and III-B. As given in Table III—for the considered settings, antennas, and frequencies—the proposed approach offers the best correction performance. The average improvement of the refined patterns w.r.t. the methods (i)–(iv) varies from 0.7 dB (Vivaldi) to 8.7 dB (monopole).

The proposed framework represents an advancement in terms of automatic postprocessing setup w.r.t. the environment. Regardless of the introduced routines, the parameters B and K that affect the correction quality are still selected based on rules-of-thumb rather than rigorous numerical analysis [13], [14], [15]. While maintaining K around a few hundred samples seems to be sufficient for high performance [13], the results of Table IV indicate that, for monopole, manually defined B yields suboptimal performance (e_R of –24.2 dB for 3 GHz versus –25.6 dB for 1.5 GHz) [13], [14]. Note that determination of suitable bandwidth is easy when the reference (i.e., AC) responses are known. Here, the tests have been performed under assumption that such a priori information is not available (as it would contradict the entire concept of postprocessing). The results show that the problem of selecting suitable B remains unsolved.

TABLE III
BENCHMARK OF THE PROPOSED METHOD

Antenna	Correction method performance (average e_R [dB])*				
	(i)	(ii)	(iii)	(iv)	This work
Vivaldi	–22.3	–22.5	–22.9	–21.7	–23.6
Monopole	–16.9	–20.9	–18.4	–23.1	–24.2

*Averaged over the center frequencies considered in Sections III.A and III.B.

TABLE IV
CORRECTION PERFORMANCE VERSUS BANDWIDTH

B [GHz]	0.5	1	1.5	2	2.5	3
Vivaldi $e_R(\boldsymbol{R}_c)$* [dB]	–23.3	–23.6	–23.1	–22.7	–22.4	–21.6
Monopole $e_R(\boldsymbol{R}_c)$* [dB]	–21.5	–24.8	–25.6	–25.5	–24.5	–24.2

*Averaged over f_0 frequencies considered in Sections III.A and III.B.

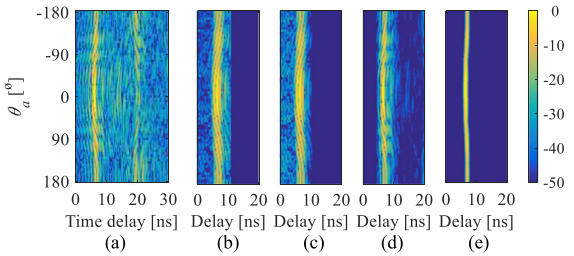

Fig. 5. Normalized PADP (in dB) of the Vivaldi antenna at $f_0 = 4$ GHz in the NA test site: (a) before, as well as after correction using (b)–(d) methods (i)–(iii), and (e) the proposed approach. Note a tight confinement of the power response in (e) and its curvature that results from the LoS profile.

Fig. 5 compares the normalized power–angle–delay profiles (PADPs) at 4 GHz for the Vivaldi antenna before and after correction using the algorithms (i)–(iii). The plots show that, among the compared time-domain algorithms, only the presented one adjusts delays based on analysis of $\boldsymbol{P}$ while ensuring tight confinement of the LoS pulse by the $\boldsymbol{T}_w$ kernel.

IV. CONCLUSION

In this letter, a wavelet-based framework for correction of far-field measurements performed in NA test sites has been proposed. The method involves automatic adjustment of the wavelet kernels w.r.t. the part of the impulse response that corresponds to the LoS transmission within the RA-AUT system. The performance of the method has been validated based on 15 experiments. For the considered test cases, the average improvement of NA radiation patterns due to the postprocessing amounts to over 10 dB. Furthermore, the method offers up to almost 9 dB better correction results compared with existing algorithms. Future work will focus on benchmark of the routine against spatial filtering and modal expansion methods.

REFERENCES

[1] L. Hemming, *Electromagnetic Anechoic Chambers: A Fundamental Design and Specification Guide*. Piscataway, NJ, USA: IEEE Press, 2002.

[2] S. Kurokawa, M. Hirose, and K. Komiyama, "Measurement and uncertainty analysis of free-space antenna factors of a log-periodic antenna using time-domain techniques," *IEEE Trans. Instrum. Meas.*, vol. 58, no. 4, pp. 1120–1125, Apr. 2009.

[3] B. Y. Toh, R. Cahill, and V. F. Fusco, "Understanding and measuring circular polarization," *IEEE Trans. Educ.*, vol. 46, no. 3, pp. 313–318, Aug. 2003.

[4] Z. Chen et al., "Compact wideband circularly polarized loop antenna based on dual common and differential modes," *IEEE Antennas Wireless Propag. Lett.*, vol. 21, no. 8, pp. 1567–1571, Aug. 2022.

[5] F.-F. Fan, Q.-L. Chen, Y.-X. Xu, X.-F. Zhao, J.-C. Feng, and Z.-H. Yan, "A wideband compact printed dipole antenna array with SICL feeding network for 5G application," *IEEE Antennas Wireless Propag. Lett.*, vol. 22, no. 2, pp. 283–287, Feb. 2023.

[6] C. Chen, "A compact wideband endfire filtering antenna inspired by a uniplanar microstrip antenna," *IEEE Antennas Wireless Propag. Lett.*, vol. 21, no. 4, pp. 853–857, Apr. 2022.

[7] S. Koziel, A. Bekasiewicz, and Q. S. Cheng, "Conceptual design and automated optimization of a novel compact UWB MIMO slot antenna," *Microw., Antennas Propag.*, vol. 11, no. 8, pp. 1162–1168, 2017.

[8] A. Rice and A. Kiourti, "High-contrast low-loss antenna: A novel antenna for efficient into-body radiation," *IEEE Trans. Antennas Propag.*, vol. 70, no. 11, pp. 10132–10140, Nov. 2022.

[9] F. G. Awan and A. Kiran, "Cancellation of interference for emission measurement in open area test site," *Measurement*, vol. 111, pp. 183–196, 2017.

[10] S. M. Froes, P. Corral, M. S. Novo, M. Aljaro, and A. C. de C. Lima, "Antenna radiation pattern measurement in a nonanechoic chamber," *IEEE Antennas Wireless Propag. Lett.*, vol. 18, no. 2, pp. 383–386, Feb. 2019.

[11] A. N. de Sao Jose, V. Deniau, U. C. Resende, and R. Adriano, "Improving antenna gain estimations in non-ideal test sites with auto-tunable filters," *Measurement*, vol. 159, 2020, Art. no. 107720.

[12] P. Piasecki and J. Strycharz, "Measurement of an omnidirectional antenna pattern in an anechoic chamber and an office room with and without time domain signal processing," in *Proc. Signal Symp.*, 2015, pp. 1–4.

[13] A. Bekasiewicz, S. Koziel, and M. Czyz, "Time-gating method with automatic calibration for accurate measurements of electrically small antenna radiation patterns in non-anechoic environments," *Measurement*, vol. 208, 2023, Art. no. 112477.

[14] S. Loredo, M. R. Pino, F. Las-Heras, and T. K. Sarkar, "Echo identification and cancellation techniques for antenna measurement in non-anechoic test sites," *IEEE Antennas Propag. Mag.*, vol. 46, no. 1, pp. 100–107, Feb. 2004.

[15] A. Soltane, G. Andrieu, E. Perrin, C. Decroze, and A. Reineix, "Antenna radiation pattern measurement in a reverberating enclosure using the time-gating technique," *IEEE Antennas Wireless Propag. Lett.*, vol. 19, no. 1, pp. 183–187, Jan. 2020.

[16] B. Fourestie, Z. Altman, J. Wiart, and A. Azoulay, "On the use of the matrix-pencil method to correlate measurements at different test sites," *IEEE Trans. Antennas Propag.*, vol. 47, no. 10, pp. 1569–1573, Oct. 1999.

[17] A. V. Oppenheim and R.W. Schafer, *Discrete-Time Signal Processing*, 3rd ed. Englewood Cliffs, NJ, USA: Prentice-Hall, 2009.

[18] M. X. Cohen, *Analyzing Neural Time Series Data: Theory and Practice*. Cambridge, MA, USA: MIT Press, 2014.

[19] J. Bai, S. Shi, and D. W. Prather, "Modified compact antipodal Vivaldi antenna for 4–50-GHz UWB application," *IEEE Trans. Microw. Theory Techn.*, vol. 59, no. 4, pp. 1051–1057, Apr. 2011.

[20] J. Hejselbaek et al., "Channel sounding system for MM-wave bands and characterization of indoor propagation at 28 GHz," *Int. J. Wireless Inf. Netw.*, vol. 24, pp. 204–216, 2017.

[21] G. Leon, S. Loredo, S. Zapatero, and F. Las-Heras, "Radiation pattern retrieval in non-anechoic chambers using the matrix pencil algorithm," *Prog. Electromagn. Res. Lett.*, vol. 9, pp. 119–127, 2009.

[22] T. K. Sarkar and O. Pereira, "Using the matrix pencil method to estimate the parameters of a sum of complex exponentials," *IEEE Antennas Propag. Mag.*, vol. 37, no. 1, pp. 48–55, Feb. 1995.

[23] H.-T. Chou and S.-J. Chou, "Multipath suppression for a 2-D antenna far-field pattern in a hybrid antenna measurement facility using the single-frequency data," *IEEE Trans. Antennas Propag.*, vol. 64, no. 9, pp. 4083–4087, Sep. 2016.

[24] T. M. Gemmer and D. Heberling, "Accurate and efficient computation of antenna measurements via spherical wave expansion," *IEEE Trans. Antennas Propag.*, vol. 68, no. 12, pp. 8266–8269, Dec. 2020.